ADVANCED MATERIALS
www.advmat.de

Check for updates

Wafer-Scale Functional Metasurfaces for Mid-Infrared Photonics and Biosensing

*Aleksandrs Leitis, Ming Lun Tseng, Aurelian John-Herpin, Yuri S. Kivshar, and Hatice Altug**

Metasurfaces have emerged as a breakthrough platform for manipulating light at the nanoscale and enabling on-demand optical functionalities for next-generation biosensing, imaging, and light-generating photonic devices. However, translating this technology to practical applications requires low-cost and high-throughput fabrication methods. Due to the limited choice of materials with suitable optical properties, it is particularly challenging to produce metasurfaces for the technologically relevant mid-infrared spectral range. These constraints are overcome by realizing functional metasurfaces on almost completely transparent free-standing metal-oxide membranes. A versatile nanofabrication process is developed and implemented for highly efficient dielectric and plasmonic mid-infrared metasurfaces with wafer-scale and complementary metal–oxide–semiconductor (CMOS)-compatible manufacturing techniques. The advantages of this method are revealed by demonstrating highly uniform and functional metasurfaces, including high-*Q* structures enabling fine spectral selectivity, large-area metalenses with diffraction-limited focusing capabilities, and birefringent metasurfaces providing polarization control at record-high conversion efficiencies. Aluminum plasmonic devices and their integration into microfluidics for real-time and label-free mid-infrared biosensing of proteins and lipid vesicles are further demonstrated. The versatility of this approach and its compatibility with mass-production processes bring infrared metasurfaces markedly closer to commercial applications, such as thermal imaging, spectroscopy, and biosensing.

1. Introduction

Metasurfaces are planar composite structures consisting of subwavelength nanoantennas or meta-atoms that can manipulate light, enabling functionalities beyond what nature provides. They can be engineered to strongly enhance light–matter interactions[1] and achieve complete control of the electromagnetic wave properties such as light phase,[2–4] amplitude,[4,5] and polarization.[2,4,6] Therefore, metasurfaces facilitate ultracompact device architectures for imaging,[7] on-chip photonic circuit integration,[8] and biochemical sensing[9–11] in spectral ranges from the ultraviolet to the mid-infrared (mid-IR). The mid-IR spectrum with wavelengths ranging from 2.5 to 25 µm is technologically important because it includes two atmospheric windows and fundamental absorption bands of chemicals and biomolecules. For these reasons, mid-IR light offers diverse applications spanning from chemical analysis and remote sensing to thermal imaging and free-space communications. For instance, IR imaging could advance optical tomography, autonomous vehicle navigation, night vision, and even food quality control. Nevertheless, developing photonic devices in this spectral range usually meets significant challenges associated with the need for unconventional materials and the limited choice of optical components.[12,13] Here, metasurfaces with their ultrathin dimensions and reduced absorption losses are very promising for mid-IR applications and could complement or even replace conventional mid-IR optical elements. However, to unleash the full potential of metasurfaces, there is an unmet need for low-cost and wafer-scale fabrication methods that can provide high flexibility, production yield, and uniformity.

Recently a lot of effort has been channeled into realizing metasurfaces and photonic devices for the visible and near-IR spectral ranges with high-throughput methods such as nanoimprint,[14,15] laser interference,[16] and deep-ultraviolet (DUV) lithography.[17,18] Most of these nanophotonic components are realized on fused silica substrates, which serve as excellent substrates for metasurfaces in the visible and near-IR wavelength ranges because of its near-zero absorption coefficient, low

A. Leitis, M. L. Tseng, A. John-Herpin, H. Altug
Institute of Bioengineering
École Polytechnique Fédérale de Lausanne (EPFL)
Lausanne 1015, Switzerland
E-mail: hatice.altug@epfl.ch

Y. S. Kivshar
Nonlinear Physics Centre
Research School of Physics
Australian National University
Canberra, Australian Capital Territory 2601, Australia

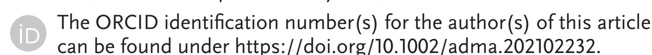
The ORCID identification number(s) for the author(s) of this article can be found under https://doi.org/10.1002/adma.202102232.

© 2021 The Authors. Advanced Materials published by Wiley-VCH GmbH. This is an open access article under the terms of the Creative Commons Attribution-NonCommercial-NoDerivs License, which permits use and distribution in any medium, provided the original work is properly cited, the use is non-commercial and no modifications or adaptations are made.

DOI: 10.1002/adma.202102232

© 2021 The Authors. Advanced Materials published by Wiley-VCH GmbH

refractive index, and sufficient mechanical durability. However, fused silica presents significant absorption losses in the mid-IR, therefore limiting its use in this spectral window. Although the operating range of metasurfaces can be extended with sapphire[19] and fluoride-based[20,21] substrates, those materials are still opaque throughout most of the mid-IR wavelength bands. Moreover, IR transparent fluoride crystals are highly brittle and therefore pose a challenge for wafer-scale fabrication. Amongst commonly used substrate materials, the high refractive index Si and Ge are prone to reflection losses, and they do not provide the much-needed refractive index contrasts between the meta-atoms and surrounding medium. Therefore, innovative fabrication approaches are needed to overcome the current limitations for producing metasurfaces with low-cost techniques for the technologically important mid-IR spectral range.

In this work, we address this long-standing challenge by introducing a versatile method for wafer-scale and cost-effective fabrication of nanophotonic metasurfaces. Our method is based on complementary metal–oxide–semiconductor (CMOS)-compatible processes in which the metasurfaces are fabricated in a high-throughput manner on silicon wafers supporting optically transparent free-standing Al_2O_3 membranes with DUV lithography. The nanoscale membranes with a thickness of ≈100 nm show high transmission and effective refractive index close to unity across a broadband range, that is, from 2 to 20 µm, thus serving as almost optically invisible substrates for metasurfaces. We demonstrate the versatility of our membrane-based fabrication method and its compatibility with a wide choice of all-dielectric and plasmonic materials by realizing mid-IR metasurfaces for a diverse range of applications. First, we validate the fabrication precision and uniformity by producing spectrally selective metasurfaces with a variance of the spectral response of less than 0.22% across the entire wafer and comparable optical performance (e.g., resonance quality factor > 100) to the counterparts fabricated with high-end electron beam lithography (EBL) methods. Additionally, we show functional dielectric metasurfaces for light wavefront and polarization control, reaching diffraction-limited focusing capabilities and polarization conversion efficiency up to 96%. Furthermore, we present large-area plasmonic metasurfaces composed of CMOS-compatible multiresonant aluminum (Al) nanoantennas. By integrating the Al-based metasurfaces into an opto-microfluidic device, we perform real-time and label-free mid-IR biosensing of the interactions between proteins and lipid vesicles. Our high-throughput fabrication method based on Al_2O_3 free-standing membranes can open a path for low-cost and mass-production of metasurfaces to enable their widespread use in mid-IR device technologies and the relevant photonic applications.

2. Nanofabrication Process Flow and Optical Properties of the Free-Standing Membranes

The reported process flow is depicted in **Figure 1**a, which starts with an atomic layer deposition (ALD) of a 100 nm thick amorphous Al_2O_3 film onto a 4 in. silicon wafer. The Al_2O_3 is selected as the membrane material due to its compelling optical[22,23] and robust mechanical properties.[24] The second step involves the deposition of a thin Al or Ge film as the plasmonic and dielectric optical material for the metasurfaces, respectively. In order to create large-area metasurfaces in a high-throughput manner, DUV lithography processes are employed by using a stepper (ASML PAS 5500/350C, KrF laser source, λ = 248 nm) to print the patterns of metasurfaces. The patterns are transferred into the metasurface material (Al or Ge) by a dry etching process. Then the metasurface layer is coated with a photoresist (PR) layer from both sides, where the front side PR serves as a protective layer for the remaining steps, and the backside-coated PR is exposed during a UV lithography step assisted by a backside alignment procedure. The UV lithography step defines the position and size of the free-standing membrane on the 4 in. wafer. The membrane-based metasurfaces are formed by removing the Si wafer material below the Al_2O_3 thin film by a deep reactive ion etching (DRIE) process. The final step involves wafer cleaning and PR removal by using oxygen plasma. The details of the fabrication method can be found in the Experimental Section.

Figure 1b displays a photograph of a fully processed 4 in. wafer consisting of multiple dielectric metasurfaces. To verify the optical properties of the free-standing membrane, we measured the transmittance of a 100 nm thick Al_2O_3 membrane over a wide spectral range using a Fourier transform infrared (FTIR) spectrometer. As shown in Figure 1c, the results indicate that the ultrathin membrane significantly reduces the absorption losses when compared to bulk sapphire substrates, which results in a near-unity transmittance over an ultrawide bandwidth spanning from 2.5 µm (5000 cm^{-1}) to 10 µm (1000 cm^{-1}) and maintains above 85% transmittance from 10 µm (1000 cm^{-1}) to 20 µm (500 cm^{-1}). Notably, the ultrathin thickness of the membrane reduces the effective refractive index of the surrounding medium down to 1.04 (Figure S1, Supporting Information), which allows achieving close to ideal metasurface performance. In general, the presence of substrate breaks the symmetry of the dielectric environment surrounding the meta-atoms, creating undesirable side effects such as resonance shift and broadening,[25] reduced efficiencies of the designed functionalities,[26–30] and unwanted interference phenomena.[25,28] In contrast, the remarkably low effective refractive index of the Al_2O_3 membranes significantly suppresses such undesired effects from conventional substrates and enables optically "free-floating" metasurface films in the air. Based on this unique configuration, we can improve the overall performance of metasurfaces (depicted in Figure 1d) for light wavefront control and biosensing.

3. High-*Q* Metasurfaces and Fabrication Uniformity

Metasurfaces that support high-quality-factor (high-*Q*) resonances provide strong electromagnetic fields, spectral selectivity and enhancement of light–matter interactions for fluorescent spectroscopy,[31] differentiation of chiral molecules,[32] and nonlinear light generation.[33] A number of mechanisms have been adopted for the designs of high-*Q* metasurfaces, which include lattice[34,35] and Fano[36,37] resonances as well as bound states in the continuum (BIC).[9,33,38] Among them, the quasi-bound states in the continuum (quasi-BIC) have attracted significant

© 2021 The Authors. Advanced Materials published by Wiley-VCH GmbH

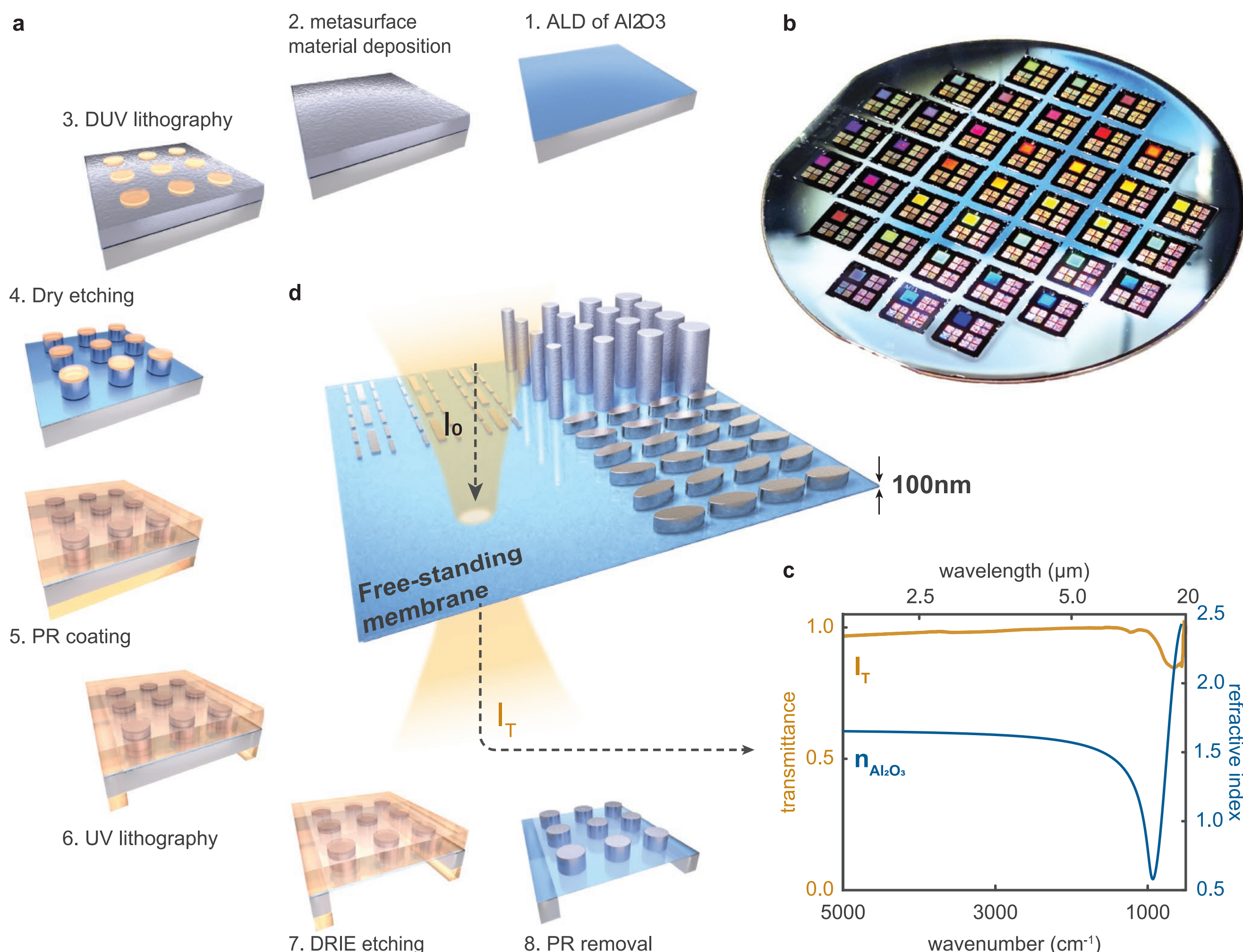

Figure 1. Wafer-scale fabrication of membrane-based metasurfaces. a) Fabrication steps of the membrane-based metasurfaces. 1) Atomic layer deposition of a 100 nm thick amorphous Al_2O_3 film. 2) Deposition of metasurface material. 3) DUV lithography for high-throughput pattern generation. 4) Dry plasma etching. 5) Photoresist coating. 6) UV laser writing for defining membrane openings. 7) Deep reactive ion etching through the wafer. 8) Oxygen plasma for resist removal. b) Photograph of a fully processed 4 in. silicon wafer consisting of large-area metasurfaces. c) Low refractive index (refractive index data are replotted from data presented in ref. [22]) and high transmittance throughout an ultrawide spectrum ranging from 2 to 20 µm make the Al_2O_3 membrane an attractive substrate material for mid-IR metasurfaces and nanophotonics. d) Illustration of various types of metasurfaces that are fabricated with the reported method, including tilted Ge ellipses supporting high-*Q* resonances, Ge nanopillars enabling wavefront and polarization control, and Al-based multiresonant plasmonic nanorod antennas for label-free biosensing.

attention recently. The utilization of quasi-BIC modes allows great flexibility for tailoring the resonance bandwidth, spectral locations, quality factor (*Q*-factor), and the distribution of the electric and magnetic fields across the meta-atoms.[39] For instance, meta-atoms that confine the fields within the resonator volume can reach *Q*-factors up to tens of thousands and are attractive for developing nanoscale light sources[40–42] and spectrally selective beam steerers.[43] Whereas metasurfaces providing strong field enhancements outside the resonator with *Q*-factors of a few hundred are compelling for sensing applications.[9,11,38] Achieving quasi-BIC modes in metasurfaces rely strongly on the precise control of the geometric parameters that can be achieved by breaking the in-plane symmetry of their meta-atoms.[39] Notably, the resonance quality and the associated field enhancements of high-*Q* metasurfaces can be affected significantly by the imperfections introduced during the fabrication processes. As a result, the high-*Q* metasurfaces have been realized primarily by low-throughput and expensive methods such as EBL.[9,32,37]

We showcase the high-throughput fabrication of all-dielectric metasurfaces supporting quasi-BIC modes on 4 in. Si wafers each containing 37 chips of the 'pixelated' metasurfaces (**Figure 2**a). A single chip with a size of 10 × 10 mm and multiple meta-atom designs is shown in Figure 2b. For a detailed chip and lithography mask layout, see Figures S2 and S3, Supporting Information. We analyze the fabrication uniformity and spectral response of the highlighted region in Figure 2b, which consists of 100 metapixels, see Figure S4, Supporting Information. Here, each metapixel is 100 × 100 µm and contains an array of elliptically shaped Ge meta-atoms in which the symmetry of the unit cell is broken through their in-plane rotations. Additionally, the unit cell size of each metapixel is scaled

 © 2021 The Authors. Advanced Materials published by Wiley-VCH GmbH

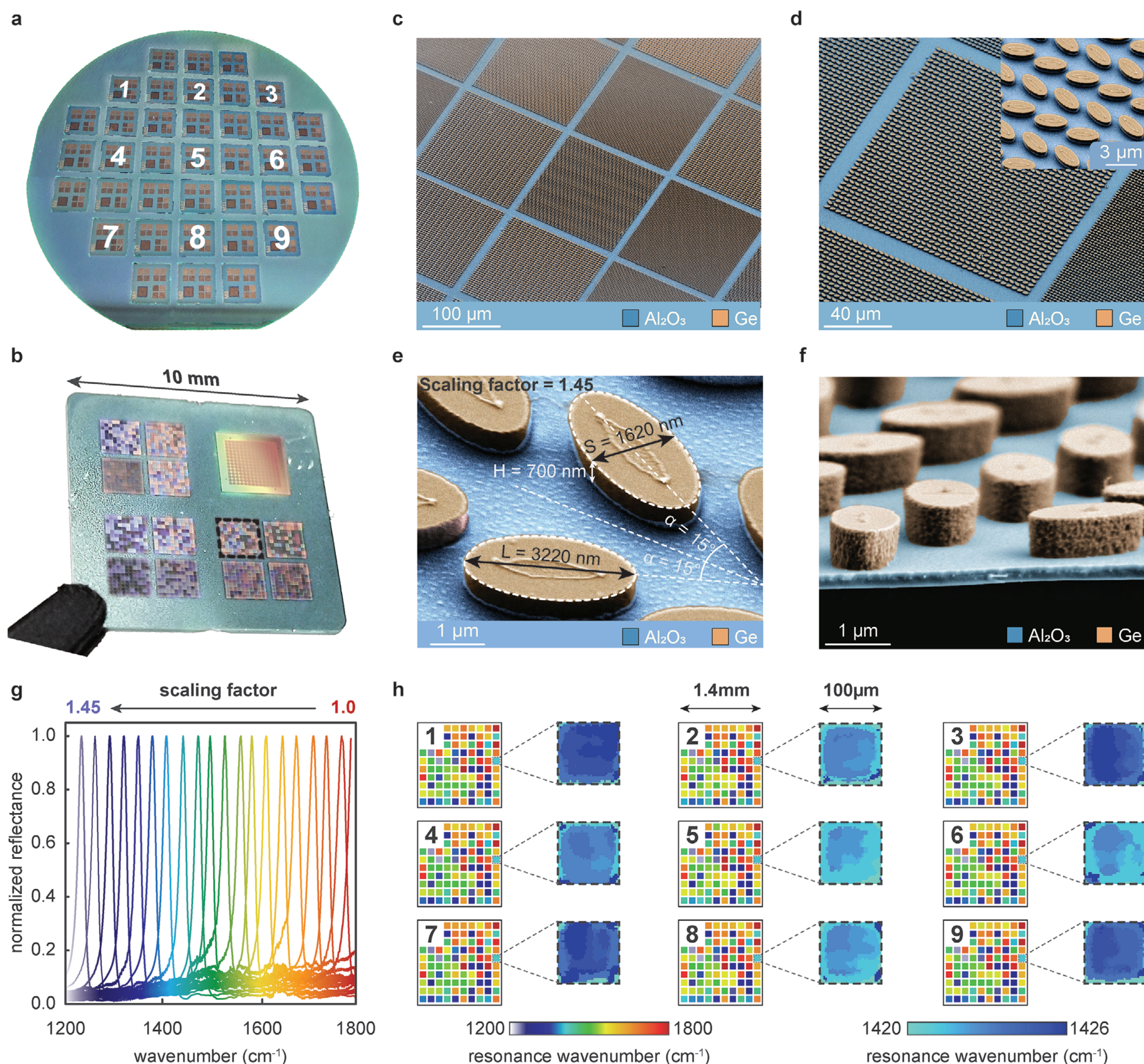

Figure 2. All-dielectric high-Q resonant metasurfaces. a) A nanopatterned standard 4 in. silicon wafer consisting of 37 pixelated dielectric metasurface chips. b) A single chip containing multiple metasurfaces. c) Color-coded SEM of high-Q pixelated dielectric metasurfaces. d) SEM of a single metapixel. Inset: Zoom-in image of the metasurface. e) High-magnification SEM image of the metasurface unit cell. f) Side view showing the thin Al_2O_3 membrane (in blue) and the Ge resonators (in orange). g) Normalized reflectance spectra of a single representative chip (from the region highlighted with black dashed lines in (b)) for every fifth metapixel out of 100, demonstrating spectrally selective resonances tuned across a wide spectrum. h) Resonance spectral position maps of the highlighted region for the nine different chips, with locations indicated in (a), demonstrate repeatability and high uniformity with a chip-to-chip spectral variance of less than 0.22%.

differently by a scaling factor (from 1 to 1.45 in 100 steps), therefore providing a broadband spectral range with high spectral resolution. Scanning electron microscopy (SEM) images show pixelated metasurface and confirm the high uniformity of the meta-atoms (Figures 2c,d). The high-magnification SEM demonstrates the precise meta-atom geometry with the specific rotation angle $\alpha = 15°$, which breaks the in-plane symmetry of the unit cell and controls the resonance Q-factor (Figure 2e). The cross-sectional SEM of the metasurface validates accurate meta-atom placement on the thin Al_2O_3 membrane (Figure 2f).

We characterized the optical performance of the pixelated metasurfaces with a tunable laser-based mid-IR microscope having a large-area hyper-spectral imaging function, see methods section. The measurement data show sharp and spectrally clean resonances that are precisely tuned from one metapixel to another over a wide wavelength range (Figure 2g). Notably, the experimental spectra are in good agreement with the numerical simulations (Figure S5, Supporting Information) and achieved resonance Q-factors ($Q \approx 100$) are comparable to similar metasurfaces made by high-resolution EBL,

© 2021 The Authors. Advanced Materials published by Wiley-VCH GmbH

see Figure S6, Supporting Information. Besides the precise replication of the meta-atom geometry, one of the important parameters of high-throughput fabrication is the uniformity of the device performance across the wafer. We measured the resonance positions of the pixelated metasurfaces over nine chips, as indicated in Figure 2a. The resonance spectral location maps of the nine chips show near identical performance (Figure 2h). We further focused on individual metapixels of each chip with a scaling factor of 1.29, which show an average resonance wavenumber of 1423 cm^{-1} (Figure 2h). Based on the spectroscopic data, the chip-to-chip spectral variance is less than 3 cm^{-1}, corresponding to less than 0.22% variation in the resonance spectral position (Figure 2h). These results confirm the high reproducibility and robustness of our fabrication process, which could be implemented toward mass-production of mid-IR metasurfaces. Furthermore, our method is compatible with different materials for the metasurface layer and the free-standing membranes. For instance, we also successfully demonstrate silicon-based high-Q metasurfaces on HfO_2 membranes, see Figure S7, Supporting Information.

4. Wavefront and Polarization Control

Meta-optics has shown a great promise for realizing photonic elements with on-demand functionalities, compact footprints, and seamless device integration for operation in transmission mode. In particular, meta-optical elements have significant potential in the infrared spectral range where they could replace the conventional bulky optical components that are usually made from delicate and unconventional materials such as CaF_2, ZnSe, and Ge by using costly fabrication techniques. However, achieving efficient and highly transmissive infrared meta-optical elements for light polarization and wavefront control is still challenging due to the limited choice of substrate materials. We tackle this problem by leveraging the unique advantages of the Al_2O_3 membranes and demonstrate two highly sought-after components, a metalens and a polarization controlling metasurface with high operation efficiencies. Such meta-optical components have the potential to replace the bulky and costly conventional mid-IR lenses and polarizers and could be readily used for miniaturized optical sensors, spectrometers, and integrated compact photonic devices.

In the metalens design, the meta-atoms are assigned as circular posts with a height of 3500 nm (**Figure 3**a) arranged in a hexagonal lattice. The symmetric shape and arrangement of the meta-atoms ensure that the resulting metalens will be insensitive to the polarization of the incident light, which is beneficial for not losing light in many practical applications. The simulation results of the transmittance and phase modulation versus the post diameter show a full 2π phase coverage with an average transmittance above 90% at the targeted working wavelength of 6.5 µm (Figure 3a, bottom). The results confirm that full wavefront control can be obtained while keeping the resulting device highly transmissive. The phase profile of the metalens is designed by considering the following equation:

$$\varphi(r) = \frac{2\pi}{\lambda}\left(\sqrt{f^2 + r^2} - f\right) \quad (1)$$

where $\varphi(r)$ is the required local phase at the radial distance of r from the center of the metalens, f is the focal length, and λ is the operational wavelength. The metalens consists of posts with different diameters that are arranged on the surface according to the calculated phase profile. The lens has a diameter of 700 µm and a designed numerical aperture (NA) of 0.36. SEM images of the metalens are presented in Figure 3b,c. Zoom-in SEM images confirm that uniform posts with a high aspect ratio were successfully produced on the free-standing membrane after the etching process. We characterized the light focusing by the metalens using our tunable laser-based mid-IR microscope at a fixed wavelength of 6.5 µm. The cross-sections of the output beam profile were recorded at different positions along the z-axis to analyze the three-dimensional propagation of the focused mid-IR beam (Figure 3d). Notably, we observed a diffraction-limited spot size with a diameter of 22.2 µm for the metalens having an NA of 0.36, transmission efficiency of 90.3%, and focusing efficiency of 70.4%, which verify the designed functionalities and the performance of the metalens (Figure S8, Supporting Information). Additionally, the size of the metalenses can be increased further. We have realized membrane-based metasurfaces with sizes larger than 1 mm (see Figure S9, Supporting Information). The sizes of membrane-based metasurfaces could be further extended with a tiling approach to centimeter-size meta-optical elements in the future.

In the case of the birefringent metasurface, it consists of elliptical posts (shown in Figure 3e), where the optical phase of one polarization component is delayed compared to the other (see Figure S10, Supporting Information). When the difference of phase delay between the orthogonal polarization components (x and y, defined in Figure 3e) is π, the metasurface rotates the polarization of the incoming light into an orthogonal state, and as a result, the birefringent metasurface operates as a $\lambda/2$ plate. On the other hand, when the phase delay difference is $\pi/2$, it turns the incoming linear polarization into a circular one, and the metasurface operates as a $\lambda/4$ plate. An SEM image of the birefringent metasurface is presented in Figure 3f. We characterized the birefringent metasurface using a tunable laser-based mid-IR microscope with an additional polarizer (analyzer) placed below the metasurface. Here, the polarization of the incoming laser light is linear and aligned to be at −45° with respect to the x-axis, see Figure 3e. The measurement data show that the metasurface performs as a $\lambda/2$ plate at 1360 cm^{-1} (7.35 µm) and rotates the polarization by 90° with 96% efficiency (Figure 3g), which is in excellent agreement with the simulation data (Figure S10, Supporting Information). Additionally, at 1440 cm^{-1} (6.95 µm), the birefringent metasurface induces a $\pi/2$ phase difference between the components and serves as a $\lambda/4$ plate. The results further point out that our method enables highly efficient metasurfaces for generating arbitrary polarization states at the targeted spectral positions. Overall, the realized meta-optical components operate with an average transmittance beyond 90%, without any anti-reflection coatings, showing that our membrane-based method is capable of producing highly efficient and transmissive metasurfaces for wavefront and polarization control in the mid-IR range.

© 2021 The Authors. Advanced Materials published by Wiley-VCH GmbH

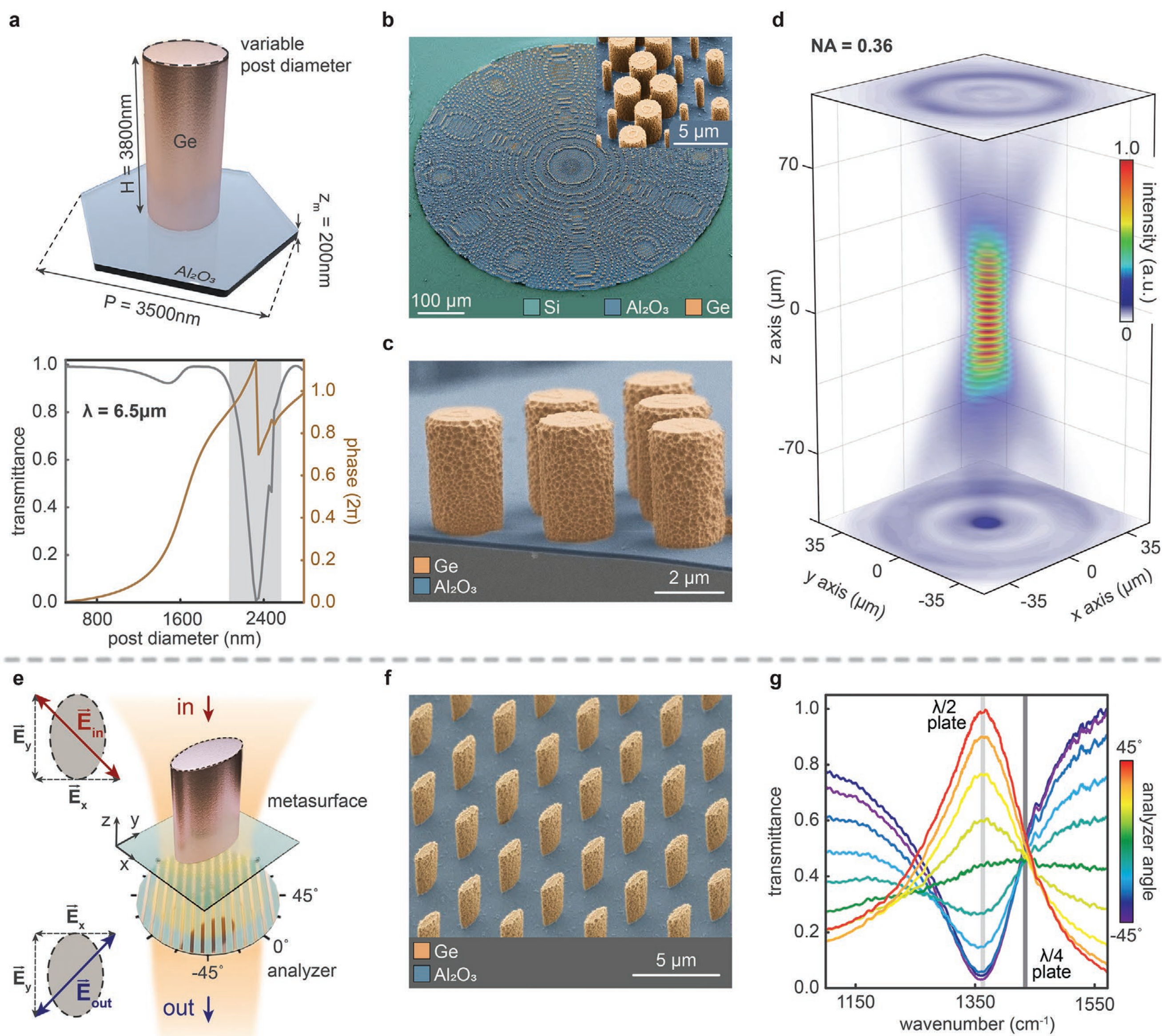

Figure 3. Highly efficient metasurfaces for wavefront shaping. a) Metasurface unit cell and numerical simulation data of the phase and transmittance for different post diameters at the operating wavelength of 6.5 µm. The shaded region indicates the post diameters that are excluded from the metalens design due to their low transmission efficiency. b) SEM images of the metalens, where the constituent materials Si, Al_2O_3, and Ge are color-coded in green, blue, and orange, respectively. c) Cross-section of the metalens with highlighted thin Al_2O_3 membrane in blue and high-aspect-ratio Ge posts in orange. d) The metalens (NA = 0.36) shows strong focusing efficiency with a diffraction-limited spot size of 22.2 µm at $\lambda = 6.5$ µm. e) Schematic drawing of the birefringent metasurface unit cell and the optical setup. f) SEM of the fabricated birefringent metasurface. g) Optical measurements of the birefringent metasurface demonstrate $\lambda/2$ plate functionalities with polarization conversion efficiency of more than 96% at 1360 cm^{-1} wavenumber ($\lambda = 7.35$ µm, light gray line). Additionally, the metasurface operates as a $\lambda/2$ plate at 1440 cm^{-1} (6.95 µm, dark gray line).

5. Plasmonic Metasurfaces and In-Flow Mid-IR Biosensing

In addition to dielectric metasurfaces, the reported wafer-scale nanofabrication method can be used for producing plasmonic metasurfaces, making it highly versatile for a diverse set of nanophotonic device applications, including biosensing.[44] A particularly interesting plasmonic material is aluminum, because, unlike the typically used Au and Ag, it is a CMOS-compatible metal capable of supporting resonances over an ultrabroad spectrum ranging from the UV to the IR.[45–49] Furthermore, Al is a low-cost and the third most abundant element on Earth.[50] Al rapidly forms a 3–5 nm-thick Al_2O_3 oxide layer in air, acting as a protecting layer, which can also be functionalized conveniently for biosensing applications.[51] Here, we designed a plasmonic metasurface consisting of Al nanoantennas, where the unit cell is based on the recently introduced self-similar multiresonant design to perform broadband biosensing using surface-enhanced IR absorption spectroscopy (SEIRA).[52] This powerful technique provides high sensitivity to

© 2021 The Authors. Advanced Materials published by Wiley-VCH GmbH

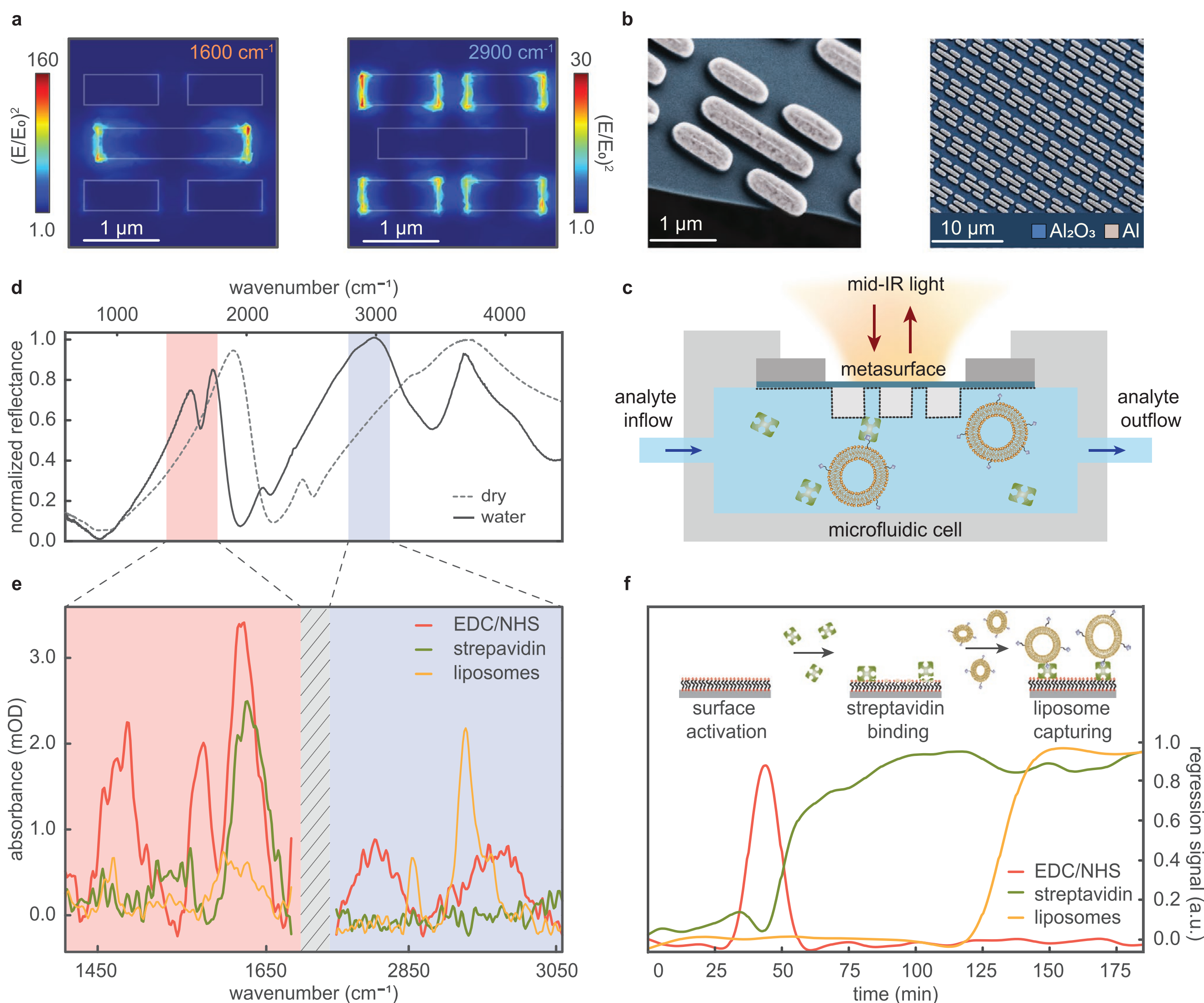

Figure 4. High-throughput and CMOS-compatible aluminum plasmonic metasurfaces for real-time optofluidic mid-IR biosensing. a) Numerical simulation data of the electric field enhancement at the two targeted resonance positions. b) SEM images of multiresonant plasmonic nanoantenna arrays. c) Illustration of the microfluidic integration with the membrane metasurface chip. d) The optical responses of the plasmonic metasurface in dry (dashed curve) and water medium (solid curve) show two strong resonances indicated by red and blue shades for simultaneous sensing of proteins and liposomes. e) Measured absorbance of the EDC/NHS surface activation molecules, streptavidin protein, and liposomes. f) Real-time regression signals of the streptavidin binding and liposome capturing events on a metasurface functionalized with phosphonic acids whose carboxyl groups were activated with an initial EDC/NHS solution. The inset schematics provide a chronological depiction of the biomolecular events where the monolayer of bound phosphonic acids on the nanoantennas is represented with three colors, that is, red for the phosphate group moieties binding to the surface, black for the alkyl chain, and orange for the carboxyl group.

detect molecules at the monolayer level via the intense electric field enhancements at the nanoantenna hotspots, which boost light–matter interaction. Operation in the mid-IR provides access to absorption ‘fingerprints’ for chemically specific and label-free molecular detection. Our nanoantennas are precisely tuned to simultaneously provide strong electric field intensity enhancements in two spectrally separate mid-IR ranges, that is, around 1600 and 2900 cm^{-1} (**Figure 4**a), to enhance overlapping absorption bands of both proteins and lipids, respectively.[53] Thus, the designed metasurface offers sensitive and label-free monitoring of interactions between proteins and lipid vesicles in real-time. We successfully fabricated these plasmonic metasurfaces on our Al_2O_3 membranes (Figure 4b), which are suitable as optical windows for in-flow experiments due to their highly transmissive and robust properties. Thereby, we can reverse the chip and mount it in a custom-built microfluidic device below a micro-FTIR objective so that the incident IR light excites the nanoantennas through the transparent membrane backside and reflects the SEIRA signal to the detector (Figure 4c). In this configuration, the incident IR light does not travel directly through the water, and only the evanescent electric field senses the water molecules, which leads to two dips in the far-field resonances without completely quenching them (Figure 4d).[54] The measured spectral response is in very good

© 2021 The Authors. Advanced Materials published by Wiley-VCH GmbH

agreement with numerical simulation data (Figure S11, Supporting Information).

We used our membrane-supported plasmonic metasurface to perform in situ real-time SEIRA measurements to observe the capturing of liposomes. These are important biomolecular entities, which are constituted of lipid molecules forming spherical-shaped vesicles, and they can encapsulate molecules, for example, for cellular communication in physiology, or for drug delivery in engineered systems. Our SEIRA experiment consists of the subsequent injections of an EDC/NHS activation solution, streptavidin proteins, and finally biotinylated liposomes onto the chip surface, which was first functionalized ex situ with a carboxyl-terminated phosphonic acid (see Figure S12, Supporting Information, and accompanying supplementary text), whose phosphate anchor groups have a strong binding affinity to various metal and metal-oxide surfaces including Al_2O_3.[51] Using reference absorption spectra for these three different analytes (Figure 4e), multiple linear regression resolves the biomolecular events on the sensor surface by tracking each analyte signal separately against time (Figure 4f).[53] In these real-time data, first, the EDC/NHS signal peaks (t = 45 min) before eventually dropping back to the baseline level. Next, the streptavidin signal starts to rise (t = 50 min) as the proteins covalently bind to the freshly activated carboxyl end groups of the phosphonic acid molecules that form the monolayer. After protein signal stabilization, the lipid signal increases (t = 130 min) with the liposomes binding to streptavidin via their displayed biotin groups. This experiment confirms the suitability of our Al-based plasmonic membrane chips for real-time, chemically specific biosensing in water. Furthermore, our metasurface sensor also offers the exciting perspective of augmenting it with deep learning algorithms to resolve even more complex biological samples.[55] Previously, EBL-fabricated Au nanoantennas on CaF_2 substrates were used for in situ SEIRA spectroscopy measurements.[10,56] Switching to a wafer-scale fabrication process flow, with a CMOS-compatible plasmonic metal such as Al, offers the prospect of mass-producible biosensor chips, which could eventually be used for disposable diagnostic devices.

6. Conclusions

We have overcome the long-term limitations for mass-producing large-area highly efficient mid-IR metasurfaces by introducing a novel approach for a CMOS-compatible fabrication method that utilizes free-standing Al_2O_3 membranes. Due to the deeply subwavelength thickness (≈2% of the operating wavelength), the membrane-based metasurfaces are optically transparent over a wide spectral range, and they have a remarkably low effective refractive index, which makes them a nearly ideal nanophotonic substrate and an optical window for various applications. The versatility of our method has been proven by realizing various types of large-area dielectric and plasmonic metasurfaces on 4 in. wafers for mid-IR photonics and biomedical spectroscopy. We have demonstrated high-Q resonant dielectric metasurfaces, highly efficient metalenses, and birefringent polarization-selective metasurfaces with record-high efficiencies. Additionally, we have incorporated aluminum-based plasmonic metasurfaces into microfluidic devices for real-time, label-free biosensing, which could be used for disposable medical devices. Considering the superior optical properties of the membranes and their compatibility with a diverse set of materials, they can be implemented in various compact and efficient photonic and micro-optical elements in a wide spectral range. Notably, although we realized the nanofabrication of large-area metasurfaces on 4 in. wafers in this work, the reported method can be seamlessly adapted for high-throughput of nanophotonic devices on the commonly used 12 in. wafers in the most advanced semiconductor foundries. Therefore, our high-throughput and cost-effective fabrication method could accelerate the adoption of metasurface photonics in the semiconductor industry and provide cutting-edge optical devices and systems for mid-IR applications.

7. Experimental Section

Numerical Simulations: The numerical simulations of the metasurface optical response were performed using CST Microwave Studio software. Ge was assumed to be lossless and had a refractive index of 4.0 in the spectral range from 5.5 to 8.5 µm, and for Al_2O_3, the optical properties were taken from Kischkat et al.[22]

Lithography Mask Fabrication: The reticle (DUV lithography mask) was realized on a 6-in. low thermal expansion quartz plate, which was coated with a 90 nm-thick layer of chromium and a 500 nm-thick PR layer (AZ1512 from MicroChemicals GmbH). The various metasurface geometries were patterned into the PR with direct UV laser writing (VPG200 from Heidelberg Instruments Mikrotechnik GmbH). Due to the DUV stepper machine's demagnification of 4×, the nanoantenna shapes on the reticle were 4× enlarged compared to the desired pattern size on the wafer. After exposure, PR was developed and, subsequently, Cr was etched. The final step included PR stripping and rinsing with deionized water.

Thin-Film Preparation: Double side polished 4 in. Si wafers were cleaned by a full standard RCA cleaning process. Al_2O_3 thin films were coated on the top of the wafers by using atomic layer deposition process (BENEQ TFS200). The films were formed on the wafer surfaces by injecting consecutive pulses of trimethyl aluminum (TMA, as precursor) and H_2O into the chamber at 200 °C. The deposition rate was 1.1 Å s^{-1}. The resulting thin films show a surface roughness of 1.5 nm.

For the pixelated metasurfaces demonstrated in Figure 2, a 700 nm Ge thin film was deposited on the Al_2O_3-coated Si wafer using an electron-beam evaporator (Leybold Optics LAB 600H). The start pressure for the material deposition was 10^{-7} mbar. The measured surface roughness of the evaporated Ge thin film was 2.27 nm. DC sputtering with Ar plasma was used to deposit Ge thin films on the wafers for wavefront shaping and polarization control metasurfaces shown in Figure 3. The start pressure for the material deposition was less than 10^{-6} mbar. The deposition rate was 6.5 Å s^{-1}, and the resulting thin films had surface roughness of 7.95 nm. For the aluminum plasmonic metasurfaces shown in Figure 4, an electron-beam evaporator (Alliance-Concept EVA 760) was used for the evaporation of 100 nm Al thin films. The deposition rate was set as 5 Å s^{-1} at the base pressure less than 10^{-7} mbar. The measured roughness of the Al thin films was found to be 1.94 nm.

Metasurface Fabrication: DUV lithography steps (anti-reflective layer and PR coating, exposure, and development) were followed on the thin films. After the development, the patterned PR was used as an etchmask for the dry etching process. Then, the metasurface was coated with an 8 µm thick PR (AZ 10XT-60) layer from both sides. A UV lithography step with backside alignment was performed using a direct laser writing lithography tool (MLA150 from Heidelberg Instruments Mikrotechnik

© 2021 The Authors. Advanced Materials published by Wiley-VCH GmbH

GmbH), after which followed the development step. In order to increase the durability and etch selectivity during the DRIE process, PR was cured at 85 °C for at least 8 h. The thin free-standing membranes were formed by removing the Si wafer material using a DRIE process until it reached the Al_2O_3 layer. The final step involved the remaining PR removal with O_2 plasma.

Optical Measurements: The free-standing membrane transmittance characterization, as well as real-time plasmonic reflectance measurements, were performed using an IR microscope (Bruker Hyperion 2000) coupled to a Fourier transform IR (FTIR) spectrometer (Bruker Vertex). The high-Q, birefringent, and optical wavefront control metasurfaces were characterized using a laser-based IR microscope (DRS Daylight Solution Spero), which was equipped with four tunable quantum cascade lasers covering the spectral range from 948 to 1800 cm^{-1} with power ranging from 2 to 9.5 mW. The microscope had two different objectives, a low magnification 0.15 NA with 2 mm field of view (FOV) and a high-magnification 0.7 NA with 0.65 mm (FOV). The 0.15 NA objective was used to characterize the high-Q and birefringent metasurfaces, which allowed simultaneous acquisition of the spectral response from all 100 metapixels. The 0.7 NA objective was used to measure the focusing beam profiles of the metalenses.

Supporting Information

Supporting Information is available from the Wiley Online Library or from the author.

Acknowledgements

A.L. and M.L.T. contributed equally to this work. The research leading to these results has received funding from the European Research Council (ERC) under grant agreement no. 682167 VIBRANT-BIO and the European Union Horizon 2020 Framework Program for Research and Innovation under grant agreements no. 665667 (call 2015), no. 777714 (NOCTURNO project). The authors also acknowledge École Polytechnique Fédérale de Lausanne and Center of MicroNano Technology for nanofabrication. Y.K. acknowledges the support from the Australian Research Council (grant DP210101292) and and the US Army International Office (grant FA520921P0034).

Conflict of Interest

The authors declare no conflict of interest.

Author Contributions

A.L. conceived the idea and with M.L.T. designed the research; A.L. fabricated the metasurfaces; A.L., A.J.-H., and M.L.T. carried out optical measurements; A.L., M.L.T. and A.J.-H. performed numerical simulations; A.L. and A.J.-H. analyzed the data; All authors contributed to writing the manuscript.

Data Availability Statement

The data that support the findings of this study are available from the corresponding author upon reasonable request.

Keywords

biosensing, CMOS compatibility, deep ultraviolet lithography, free-standing membranes, high-throughput fabrication, metasurfaces, wavefront and polarization control

Received: March 22, 2021
Revised: June 23, 2021
Published online:

[1] J. A. Schuller, E. S. Barnard, W. Cai, Y. C. Jun, J. S. White, M. L. Brongersma, *Nat. Mater.* **2010**, *9*, 193.
[2] A. Arbabi, Y. Horie, M. Bagheri, A. Faraon, *Nat. Nanotechnol.* **2015**, *10*, 937.
[3] N. Yu, F. Capasso, *Nat. Mater.* **2014**, *13*, 139.
[4] M. K. Chen, Y. Wu, L. Feng, Q. Fan, M. Lu, T. Xu, D. P. Tsai, *Adv. Opt. Mater.* **2021**, *9*, 2001414.
[5] N. Liu, M. Mesch, T. Weiss, M. Hentschel, H. Giessen, *Nano Lett.* **2010**, *10*, 2342.
[6] N. Yu, F. Aieta, P. Genevet, M. A. Kats, Z. Gaburro, F. Capasso, *Nano Lett.* **2012**, *12*, 6328.
[7] F. Capasso, M. Khorasaninejad, W. T. Chen, R. C. Devlin, J. Oh, A. Y. Zhu, *Science* **2016**, *352*, 1190.
[8] S. A. Maier, M. L. Brongersma, P. G. Kik, S. Meltzer, A. A. G. Requicha, H. A. Atwater, *Adv. Mater.* **2001**, *13*, 1501.
[9] A. Leitis, A. Tittl, M. Liu, B. H. Lee, M. B. Gu, Y. S. Kivshar, H. Altug, *Sci. Adv.* **2019**, *5*, eaaw2871.
[10] A. Tittl, A. John-Herpin, A. Leitis, E. R. Arvelo, H. Altug, *Angew. Chem., Int. Ed.* **2019**, *58*, 14810.
[11] M. L. Tseng, Y. Jahani, A. Leitis, H. Altug, *ACS Photonics* **2020**, *8*, 47.
[12] H. Lin, Z. Luo, T. Gu, L. C. Kimerling, K. Wada, A. Agarwal, J. Hu, *Nanophotonics* **2017**, *7*, 393.
[13] A. Mann, *Infrared Optics and Zoom Lenses*, SPIE Press, Bellingham, WA, USA **2010**, pp. 25–33.
[14] G. Yoon, K. Kim, D. Huh, H. Lee, J. Rho, *Nat. Commun.* **2020**, *11*, 2268.
[15] T. D. Gupta, L. Martin-Monier, W. Yan, A. L.e Bris, T. Nguyen-Dang, A. G. Page, K. T. Ho, F. Yesilköy, H. Altug, Y. Qu, F. Sorin, *Nat. Nanotechnol.* **2019**, *14*, 320.
[16] J. Berzinš, S. Indrišiūnas, K. Van Erve, A. Nagarajan, S. Fasold, M. Steinert, G. Gerini, P. Gečys, T. Pertsch, S. M. B. Bäumer, F. Setzpfandt, *ACS Nano* **2020**, *14*, 6138.
[17] W. Bogaerts, V. Wiaux, D. Taillaert, S. Beckx, B. Luyssaert, P. Bienstman, R. Baets, *IEEE J. Sel. Top. Quantum Electron.* **2002**, *8*, 928.
[18] J. S. Park, S. Zhang, A. She, W. T. Chen, P. Lin, K. M. A. Yousef, J. X. Cheng, F. Capasso, *Nano Lett.* **2019**, *19*, 8673.
[19] A. Arbabi, R. M. Briggs, Y. Horie, M. Bagheri, A. Faraon, *Opt. Express* **2015**, *23*, 33310.
[20] H. Zuo, D. Y. Choi, X. Gai, P. Ma, L. Xu, D. N. Neshev, B. Zhang, B. Luther-Davies, *Adv. Opt. Mater.* **2017**, *5*, 1700585.
[21] L. Zhang, J. Ding, H. Zheng, S. An, H. Lin, B. Zheng, Q. Du, G. Yin, J. Michon, Y. Zhang, Z. Fang, M. Y. Shalaginov, L. Deng, T. Gu, H. Zhang, J. Hu, *Nat. Commun.* **2018**, *9*, 1481.
[22] J. Kischkat, S. Peters, B. Gruska, M. Semtsiv, M. Chashnikova, M. Klinkmüller, O. Fedosenko, S. MacHulik, A. Aleksandrova, G. Monastyrskyi, Y. Flores, W. T. Masselink, *Appl. Opt.* **2012**, *51*, 6789.
[23] H. J. Hagemann, W. Gudat, C. Kunz, *J. Opt. Soc. Am.* **1975**, *65*, 742.
[24] M. Berdova, O. M. E. Ylivaara, V. Rontu, P. T. Törmä, R. L. Puurunen, S. Franssila, *J. Vac. Sci. Technol., A* **2015**, *33*, 01A106.
[25] J. van de Groep, A. Polman, *Opt. Express* **2013**, *21*, 26285.

© 2021 The Authors. Advanced Materials published by Wiley-VCH GmbH

[26] H. Liang, A. Martins, B.-H. V. Borges, J. Zhou, E. R. Martins, J. Li, T. F. Krauss, *Optica* **2019**, *6*, 1461.
[27] M. Decker, I. Staude, M. Falkner, J. Dominguez, D. N. Neshev, I. Brener, T. Pertsch, Y. S. Kivshar, *Adv. Opt. Mater.* **2015**, *3*, 813.
[28] Q. Yang, S. Kruk, Y. Xu, Q. Wang, Y. K. Srivastava, K. Koshelev, I. Kravchenko, R. Singh, J. Han, Y. Kivshar, I. Shadrivov, *Adv. Funct. Mater.* **2020**, *30*, 1906851.
[29] A. Leitis, A. Heßler, S. Wahl, M. Wuttig, T. Taubner, A. Tittl, H. Altug, *Adv. Funct. Mater.* **2020**, *30*, 1910259.
[30] A. Arbabi, A. Faraon, *Sci. Rep.* **2017**, *7*, 43722.
[31] S. Yuan, X. Qiu, C. Cui, L. Zhu, Y. Wang, Y. Li, J. Song, Q. Huang, J. Xia, *ACS Nano* **2017**, *11*, 10704.
[32] J. Hu, M. Lawrence, J. A. Dionne, *ACS Photonics* **2020**, *7*, 36.
[33] Z. Liu, Y. Xu, Y. Lin, J. Xiang, T. Feng, Q. Cao, J. Li, S. Lan, J. Liu, *Phys. Rev. Lett.* **2019**, *123*, 253901.
[34] V. G. Kravets, A. V. Kabashin, W. L. Barnes, A. N. Grigorenko, *Chem. Rev.* **2018**, *118*, 5912.
[35] W. Zhou, M. Dridi, J. Y. Suh, C. H. Kim, D. T. Co, M. R. Wasielewski, G. C. Schatz, T. W. Odom, *Nat. Nanotechnol.* **2013**, *8*, 506.
[36] M. F. Limonov, M. V. Rybin, A. N. Poddubny, Y. S. Kivshar, *Nat. Photonics* **2017**, *11*, 543.
[37] B. Luk'yanchuk, N. I. Zheludev, S. A. Maier, N. J. Halas, P. Nordlander, H. Giessen, C. T. Chong, *Nat. Mater.* **2010**, *9*, 707.
[38] A. Tittl, A. Leitis, M. Liu, F. Yesilkoy, D.-Y. Choi, D. N. Neshev, Y. S. Kivshar, H. Altug, *Science* **2018**, *360*, 1105.
[39] K. Koshelev, S. Lepeshov, M. Liu, A. Bogdanov, Y. Kivshar, *Phys. Rev. Lett.* **2018**, *121*, 193903.
[40] C. Huang, C. Zhang, S. Xiao, Y. Wang, Y. Fan, Y. Liu, N. Zhang, G. Qu, H. Ji, J. Han, L. Ge, Y. Kivshar, Q. Song, *Science* **2020**, *367*, 1018.
[41] S. T. Ha, Y. H. Fu, N. K. Emani, Z. Pan, R. M. Bakker, R. Paniagua-Domínguez, A. I. Kuznetsov, *Nat. Nanotechnol.* **2018**, *13*, 1042.
[42] K. Koshelev, S. Kruk, E. Melik-Gaykazyan, J. H. Choi, A. Bogdanov, H. G. Park, Y. Kivshar, *Science* **2020**, *367*, 288.
[43] M. Lawrence, D. R. Barton, J. Dixon, J. H. Song, J. van de Groep, M. L. Brongersma, J. A. Dionne, *Nat. Nanotechnol.* **2020**, *15*, 956.
[44] A. V. Kabashin, P. Evans, S. Pastkovsky, W. Hendren, G. A. Wurtz, R. Atkinson, R. Pollard, V. A. Podolskiy, A. V. Zayats, *Nat. Mater.* **2009**, *8*, 867.
[45] M. W. Knight, N. S. King, L. Liu, H. O. Everitt, P. Nordlander, N. J. Halas, *ACS Nano* **2014**, *8*, 834.
[46] D. Gerard, S. K. Gray, *J. Phys. D: Appl. Phys.* **2015**, *48*, 184001.
[47] B. Cerjan, X. Yang, P. Nordlander, N. J. Halas, *ACS Photonics* **2016**, *3*, 354.
[48] S. S. Raja, C. W. Cheng, Y. Sang, C. A. Chen, X. Q. Zhang, A. Dubey, T. J. Yen, Y. M. Chang, Y. H. Lee, S. Gwo, *ACS Nano* **2020**, *14*, 8838.
[49] H. W. Liu, F. C. Lin, S. W. Lin, J. Y. Wu, B. T. Chou, K. J. Lai, S. Di Lin, J. S. Huang, *ACS Nano* **2015**, *9*, 3875.
[50] M. W. Knight, L. Liu, Y. Wang, L. Brown, S. Mukherjee, N. S. King, H. O. Everitt, P. Nordlander, N. J. Halas, *Nano Lett.* **2012**, *12*, 6000.
[51] K. Chen, T. D. Dao, S. Ishii, M. Aono, T. Nagao, *Adv. Funct. Mater.* **2015**, *25*, 6637.
[52] D. Rodrigo, A. Tittl, A. John-Herpin, O. Limaj, H. Altug, *ACS Photonics* **2018**, *5*, 4903.
[53] D. Rodrigo, A. Tittl, N. Ait-Bouziad, A. John-Herpin, O. Limaj, C. Kelly, D. Yoo, N. J. Wittenberg, S. H. Oh, H. A. Lashuel, H. Altug, *Nat. Commun.* **2018**, *9*, 2160.
[54] R. Adato, H. Altug, *Nat. Commun.* **2013**, *4*, 2154.
[55] A. John-herpin, D. Kavungal, L. Von Mücke, H. Altug, *Adv. Mater.* **2021**, *33*, 2006054.
[56] F. Neubrech, C. Huck, K. Weber, A. Pucci, H. Giessen, *Chem. Rev.* **2017**, *117*, 5110.

© 2021 The Authors. Advanced Materials published by Wiley-VCH GmbH